PAPER

Check for updates

Coupled morphological and structural evolution of δ-MnO₂ to α-MnO₂ through multistage oriented assembly processes: the role of Mn(III)†

Xinran Liang, [iD] [ab] Jeffrey E. Post,[c] Bruno Lanson, [iD] [d] Xiaoming Wang, [iD] [a] Mengqiang Zhu, [iD] [e] Fan Liu,[a] Wenfeng Tan, [iD] [a] Xionghan Feng, [iD] *[a] Guomin Zhu,[b] Xin Zhang[b] and James. J. De Yoreo[b]

α-MnO₂ is a typical tunneled Mn oxide (TMO) that is frequently associated with δ-MnO₂ in the environment and exhibits strong adsorption and oxidation activity. The morphology of α-MnO₂, which is controlled by an oriented attachment (OA) process, is one of the key factors affecting its reactivity. However, the detailed crystal growth process and coupling between morphology and structure of α-MnO₂ during OA processes remain poorly understood. We propose that the transformation of layer-based δ-MnO₂ to tunnel-based α-MnO₂ occurs *via* a multistage OA process. In the initial stage, the produced δ-MnO₂ nanoflakes are found to spontaneously self-assemble into a nanoribbon with a large number of lattice defects *via* edge-to-edge OA. The presence of lattice defects promotes the generation of oxygen vacancies, and the Mn(IV) ions in the [MnO₆] octahedral layers of δ-MnO₂ are reduced to Mn(III)/Mn(II). The reduced ions subsequently migrate from the [MnO₆] octahedral layers to the interlayers during this process. The hydroxide which acts in coordination with the interlayer Mn(III)/Mn(II) and oxygen atoms coordination with adjacent nanoribbons attach to each other driven by hydrogen bonding and form primary nanorods through a face-to-face OA mechanism along the *c*-axis. Concomitantly, the bonding of [Mn(III)O₆] octahedra in the interlayer of the nanoribbons with adjacent [MnO₆] octahedral layers leads to the fabrication of a new α-MnO₂ tunnel structure from the original δ-MnO₂. These findings provide insights into both the transformation mechanisms of the layer-based to the tunnel-based nanoparticles and methods for the efficient and controlled synthesis of nanomaterials.

Environmental significance

δ-MnO₂ and α-MnO₂ are widespread near and on the earth's surface and play an important role in elemental cycles and pollutant dynamics. These behaviors are closely related to the structure and morphology of the minerals. Although documented in the literature, α-MnO₂ nanorod crystal growth processes and the relationship between the structural transformation and morphological evolution are not clearly understood. In this study, the transformation of the layer-based δ-MnO₂ to tunnel-based α-MnO₂ is found to occur *via* a multistage OA process. The disordered structure produced by δ-MnO₂ nanoflakes *via* the OA process facilitates the reduction of Mn(IV) in the layer to Mn(III), and Mn(III) migrates out to the interlayer. Interlayer Mn(III) promotes the face-to-face OA of adjacent nanoribbons to form a nanorod and to form a 2 × 2 α-MnO₂ tunnel structure as tunnel "walls". These findings provide insights into not only the transformation mechanisms of layer-based to tunnel-based nanoparticles in the environment but also the efficient and controlled synthesis of environmentally friendly materials.

[a] Key Laboratory of Arable Land Conservation (Middle and Lower Reaches of Yangtze River), Ministry of Agriculture, College of Resources and Environment, Huazhong Agricultural University, Wuhan 430070, China. E-mail: fxh73@mail.hzau.edu.cn
[b] Physical Sciences Division, Pacific Northwest National Laboratory, Richland, WA 99352, USA
[c] Department of Mineral Sciences, Smithsonian Institution, Washington, DC 20013, USA
[d] University of Grenoble Alpes, CNRS, ISTerre, F-38000 Grenoble, France
[e] Department of Ecosystem Science and Management, University of Wyoming, Laramie, WY, 82071, USA
† Electronic supplementary information (ESI) available. See DOI: 10.1039/c9en01000a

Introduction

Oriented attachment (OA) is a nonclassical mechanism of crystal growth, and it proceeds by repeated attachment events of crystalline particles on specific crystal faces that are lattice-matched with true crystallographic alignment.[1] The growth of many crystalline substances, including engineered nanomaterials and natural nanoparticles, has been reported to occur *via* the OA mechanism.[2] The properties of these nanoparticles are closely related to their morphologies and structures. The OA process only leads to morphological

238 | *Environ. Sci.: Nano*, 2020, **7**, 238–249

This journal is © The Royal Society of Chemistry 2020

evolution, as indicated in previous reports, while the processes of structural changes associated with morphological evolutions have been explored to a lesser extent.[1,2] Revealing the relationship between morphological evolution and structural changes during the OA process is not only important for controlling the growth of synthetic materials but also for providing novel ideas for the study of crystal growth.[3]

Recent studies have reported that poor crystallinity layer manganese oxide (LMO) nanoparticles assemble as LMO nanoflowers and tunneled manganese oxide (TMO) nanorods *via* the OA mechanism.[4–8] LMO-to-TMO reaction mechanisms have been extensively investigated because LMO association with TMOs occurs frequently in the environment.[5,8–10] In addition, LMOs and TMOs have also been extensively applied as materials in catalysis, ion exchange, energy storage, and octahedral molecular sieves.[9,10] There are some detailed studies on their structural evolution and a few studies on the morphological evolution during LMO-to-TMO reactions.[8,11] The two separate studies on the structural and morphological evolution indicate that there are some difficulties in understanding their relationship and the reaction mechanism of the LMO-to-TMO process in the environment.

In the natural environment, cryptomelane (α-MnO$_2$) represents an important family of TMOs with 2×2 and 1×1 (intergrowth little 2×3, 2×4 and "T" junction structure, *etc.*) tunnel structures, which are formed when double chains of edge-sharing [MnO$_6$] octahedra share corners with neighboring chains (Fig. S1†).[12,13] The larger tunnels are generally stabilized by K$^+$, Ba$^+$, and Na$^+$.[14] Cryptomelane is the major manganese oxide in the supergene oxidation zones of Mn-bearing crusts and manganese deposits and lateritic weathered profiles.[15–17] The unique physicochemical properties of α-MnO$_2$ have provided a wide range of potential applications in removing environment pollutions.[18–20] These applications are considerably affected by the structure and morphology of α-MnO$_2$.[20]

δ-MnO$_2$ (Fig. S1B†) is the most common LMO in the environment, with strong adsorption and oxidation activity frequently associated with α-MnO$_2$.[11] It was proposed that the formation and migration of Mn(III) occurred while δ-MnO$_2$ transformed to α-MnO$_2$.[21] Yuan *et al.* also reported the transforming process of highly crystalline buserite to todorokite (2×3 tunnel structure) through Mn(III) migration by the combination of morphology, structure and theoretical calculation studies.[20] Additionally, a detailed OA process based on the formation of long α-MnO$_2$ nanorods from α-MnO$_2$ primary nanorods was also reported.[20,22–24] However, the formation process of the primary α-MnO$_2$ nanorods from poor crystallinity δ-MnO$_2$ nanoparticles is still unknown due to the too fast or slow conversion rates under different reaction conditions, which are detrimental to the capture of the transition state.[12,13] In addition, it is unclear how the new tunnel structure formation corresponds with the morphological evolution by the OA process. A basic knowledge of the morphological evolution across the entire synthetic process and the relationship with the structural transformation is also critical for

α-MnO$_2$ material synthesis in various applications, and the understanding of the minerology and behavior of different types of MnO$_2$ minerals in nature.

In this study, Na$^+$/K$^+$-stabilized α-MnO$_2$, similar to environmental cryptomelane nanorods, was synthesized by co-precipitation of Na/KMnO$_4$ with MnSO$_4$. The dynamic process of the formation of the Na$^+$-stabilized α-MnO$_2$ nanorods was carefully explored. Given that the Na$^+$-stabilized α-MnO$_2$ forms at a slower rate compared to that of K$^+$, as shown in previous experiments, it provides a more suitable system for the investigation of the process of α-MnO$_2$ formation.[14] During the synthesis, intermediate products were sampled and quenched in liquid N$_2$ at different time intervals to stop crystal growth and to capture *in situ* morphologies and structures. These intermediate samples were characterized by using the pair distribution function (PDF), and X-ray photoelectron spectroscopy (XPS), to illustrate the structural changes at the atomic level. Meanwhile, morphological changes during the formation process were revealed with the use of high-resolution transmission electron microscopy (HRTEM) and field-emission scanning electron microscopy (FESEM). Possible mechanisms for the observed relationship between morphological and structural evolutions are proposed.

Experimental section

Synthesis of different types of cations of α-MnO$_2$

In a typical experiment, 8.45 g of MnSO$_4$·H$_2$O (0.5 M) in 100 mL of acetic acid (2 M) and 80 mL of an aqueous solution of AMnO$_4$ (0.4375 M, A = K or Na) were mixed together under vigorous stirring at 60 °C. This suspension was heated to 100 °C for 20 min and was then cooled to 80 °C in open air. After cooling to 80 °C, the suspension was frozen by liquid nitrogen and washed until the conductivity of the supernatant was less than 20.0 μS cm^{-1}; the suspension was then freeze-dried.[25]

After the two solutions were mixed and the suspension was heated to 100 °C, 10 mL of the suspension was extracted into a 50 mL centrifuge tube filled with 20 mL of liquid nitrogen at 0, 2, 4, 6, 8, 10, 14, 16 and 20 min. The extracted samples were centrifuged at 12 000 rpm for 8 min and the precipitates were washed with 50 mL of DDW multiple times until the conductivity of the supernatant was less than 20.0 μS cm^{-1}. The precipitates were then freeze-dried for characterization. Samples were labelled AMix, A100-X and A80, where X is the heating time at 100 °C and A is the type of cation.

Powder X-ray diffraction (PXRD)

PXRD patterns were collected from the dried powders using a cavity mount on a Bruker D8 Advance diffractometer equipped with a LynxEye detector, using Ni-filtered Cu Kα radiation (λ = 0.15418 nm). The diffractometer was operated at a tube voltage of 40 kV and a current of 40 mA, with a scanning rate of 1° min^{-1} and a step size of 0.02°.

This journal is © The Royal Society of Chemistry 2020

Environ. Sci.: Nano, 2020, **7**, 238–249 | **239**

Elemental analysis and Mn AOS

The chemical composition of the samples was determined by dissolving ~0.1 g of each powder sample in 25 mL of 0.25 mol L^{-1} $NH_2OH \cdot HCl$. The concentrations of dissolved Mn and K were measured using inductively coupled plasma (ICP) and flame spectrometry, respectively. Mn average oxidation state (AOS) was measured by a back-titration method using a $KMnO_4$ standard solution.[26]

X-ray photoelectron spectroscopy

X-ray photoelectron spectra were collected using a VG Multilab2000 X-ray photoelectron spectrometer with an Al K X-ray source (1486 eV) and a base pressure of 3×10^{-9} Torr in the analytical chamber. The scans were recorded using the large area mode. The survey scans were collected using a fixed pass energy of 100 eV and an energy step size of 1.0 eV, whereas the narrow scans have a pass energy of 25 eV and an energy step size of 0.1 eV. The charge effect was corrected by adjusting the binding energy (BE) of C (1 s) to 284.62 eV. The spectra were analyzed using the Avantage software. The Shirley-type background was subtracted before deconvolution and fitting. The parameters used by Iton et al. for the multiple peaks of Mn ($2p_{3/2}$) and Mn 3s for spectral fitting were adopted.[27] A 20:80 ratio of the Lorentzian:Gaussian mixsum function was used for all the fittings.

Transmission electron microscopy

The particle size and morphology of the samples were further examined on a JEM-2100F transmission electron microscope and by using FEI Titan 80/300 environmental transmission electron microscopy. Prior to observation, samples were embedded in epoxy resin, left to polymerize for 48 h in the dark and cut with an ultramicrotome (Leica EM UC6) equipped with a diamond knife. The ~50 nm thick sections were picked up on lacey carbon films loaded on Cu grids. In addition, to assess possible preparation-induced artefacts (use of an ultramicrotome), all samples were prepared according to the above described protocol, filtered and re-suspended in ethanol. A drop of the obtained suspension was deposited on a copper microscope grid covered with perforated carbon.

Atomic force microscopy

All of the images were recorded in air using tapping mode on a MultiMode VIII AFM (Bruker, CA). Rfespa-190 probes (Bruker, CA) were used in the experiment. The raw data were further analyzed using NanoScope Analysis v 1.50 offline software (Bruker, CA).

Field-emission scanning electron microscopy

Detailed three-dimensional morphologies of particles were observed by using a field emission scanning electron microscope (SU8010, Hitachi) with a maximum resolution of 1 nm. For high-resolution SEM, the microscope was operated at 15 kV and the working distance was 0.5–30 mm; an in-lens secondary electron detector was used. Prior to SEM analysis, each sample was gold-coated.

## High-energy X-ray total scattering

Synchrotron-based X-ray total scattering data were collected using an X-ray energy of 58.6491 keV (λ = 0.2114 Å) at beamline 11-ID-B of the Advanced Photon Source (APS), Argonne National Laboratory (APS). The measurement was performed using the rapid acquisition PDF method by employing a Perkin Elmer amorphous silicon detector. The image plate was exposed for 1.2 s and the measurement was repeated 75 times for a total collection time of 90 s for each sample. The software Fit2D was used to integrate and convert the 2-D raw data to 1-D intensity versus wave vector (Q) data. The PDF, $G(r)$, was obtained from the raw 1-D data using the program PDFgetX2.

Results and discussion

During the synthesis of δ-MnO_2, the amount of added MnO_4^- was in excess relative to the stoichiometric ratio of Mn(II), as shown in eqn (1).

$$2MnO_4^- + 3Mn^{2+} + 2H_2O \rightarrow 5\delta\text{-}MnO_2 + 4H^+ \qquad (1)$$
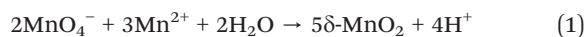
Therefore, the supernatant color changed to purple after the two solutions were mixed. After the solution was heated to 100 °C for 14 min, the color of the supernatant changed from purple to colorless owing to the complete reduction of the MnO_4^- ions under acidic conditions (pH = 0.86) according to eqn (2).[22,28]

$$4MnO_4^- + 4H^+ \rightarrow 4\delta\text{-}MnO_2 + 3O_2 + 2H_2O \qquad (2)$$
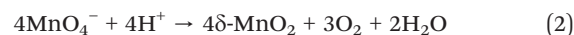
Morphological evolution

HRTEM, FESEM, and electron diffraction were used to elucidate the kinetics of the morphological evolution during the phase transformation. After $NaMnO_4$ and $MnSO_4$ were mixed, a three-dimensional morphology of aggregation of approximately 100 nm in width was observed (Fig. S2A†), and primary nanoflakes were observed using HRTEM after ultrasonic dispersion (Fig. 1A and B). This indicates that the primary nanoflakes aggregated loosely driven by the surface energy. The edges of the primary nanoflakes were approximately 3 to 4 nm (Fig. 1B and S4†). The lattice cannot be observed in Fig. 1B owing to the poor crystallinity of the nanoflakes. Furthermore, the selected area diffraction (SAED) pattern (inset of Fig. 1B) shows two diffuse diffraction rings at ~0.24 nm and ~0.14 nm, which is consistent with the $d_{(100)}$ = 0.24 nm and $d_{(110)}$ = 0.14 nm spacings of δ-MnO_2, respectively. Additionally, the absence of the (001) and (002) diffraction rings in the SAED pattern indicates that at this stage, the poorly crystallized nanoflakes consist of no more than a few $[MnO_6]$ octahedral layers. The atomic force microscopy (AFM) results
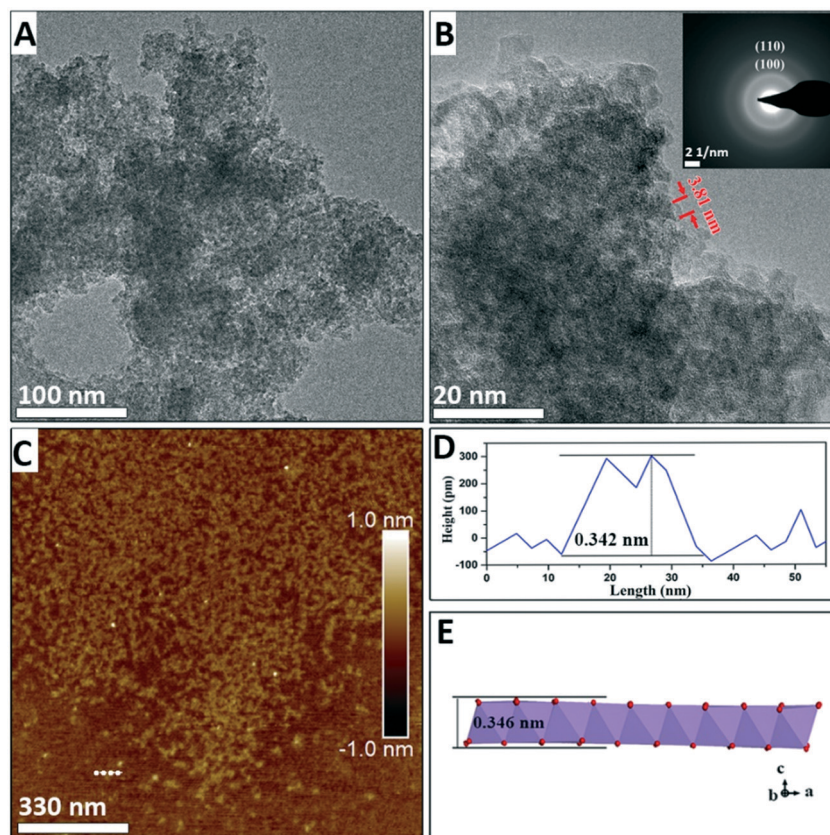
Fig. 1 TEM images of intermediate product of NaMix (A and B) and the SAED pattern (B inset) recorded by focusing the electron beam in the area of image B. AFM image (C) of the intermediate product of NaMix. Profile image (D) corresponds to the trajectory shown in Fig. 1C. (E) Schematic of single layer δ-MnO$_2$.

in Fig. 1C show two-dimensional nanoflakes with an average height of approximately 0.35 nm (Fig. 1D), which is consistent with the thickness of a single [MnO$_6$] octahedral layer.

When the suspension is heated for 6 min, nanoribbons appear (with lengths ranging from 20 to 60 nm and widths from 3 to 7 nm, as shown in Fig. 2A and B). In addition, the nanoribbon is aggregated from many nanoflakes, as shown in Fig. 2B and C. A diffraction ring is also observed in the SAED pattern at ~0.14 nm and ~0.24 nm and it originates from the (110) and (100) reflections of δ-MnO$_2$ (inset of Fig. 2B). Although the morphology changes, no other diffraction peaks appear. The thickness of the nanoribbon in Fig. 2C is only 0.356 nm, which confirms that the nanoribbons maintain a single-layer δ-MnO$_2$ structure. The assembly of δ-MnO$_2$ at low pH is energetically favored because the primary nanoflakes have high-surface energy, low-Na$^+$ content, and hydroxyls on edge sites that can generate hydrogen bonding with the adjacent nanoflakes.[4]

When the suspension is heated for 10 min, the width and length of the nanoribbons increase to ~30 nm and ~100 nm, respectively (Fig. 3A). HRTEM images show in the sectioning of the nanosheets along the (001) plane in Fig. 3B that nanoribbons are thickened by the assembly and form nanorods with a thickness of ~7 nm (the sectioning schematic along the (001) plane is shown in Fig. S3A†). The measured d_{hkl}

spacing of 0.69 nm corresponds to the (110) plane of α-MnO$_2$ in Fig. 3D. The observed nanorods exhibit different sizes and crystallographic orientations owing to the assembly of multiple primary nanorods (Fig. 3B). The nanoribbons are cut off in the [110] direction (as shown in Fig. 3C, and the cutting schematic along the (001) plane is shown in Fig. S3B†). It is shown that the length of the nanoribbons is ~40 nm. However, the observed thickness of the nanoribbons (2.24 nm) corresponds to only three [MnO$_6$] octahedral layers. The top [MnO$_6$] octahedral layer assembled on the nanosheet has a d spacing of 1.00 nm, which is larger than the $d_{(110)}$ value of the lower layer (Fig. 3C). Furthermore, the size of this layer shown in blue squares in Fig. 3C is 6.7 nm, which corresponds to the typical lateral dimensions of the nanoflakes, and indicates that the nanoribbons thicken by the face-to-face assembling of the nanoflakes. The AFM image in Fig. S5B† also reveals the assembly of the nanoflakes on the nanoribbons. The blue circles in Fig. 3C mark the dislocations along the [001] and [110] directions. Because the dislocations are a common remnant of attachment events, these may indicate the attachment of two small nanorods assembled by both end-to-end (along the (001) plane) and side-to-side OA (along the (110) plane).[20] HRTEM shows that the nanorods have serrated sides that may form during the assembly of the nanoflakes (Fig. 3D).
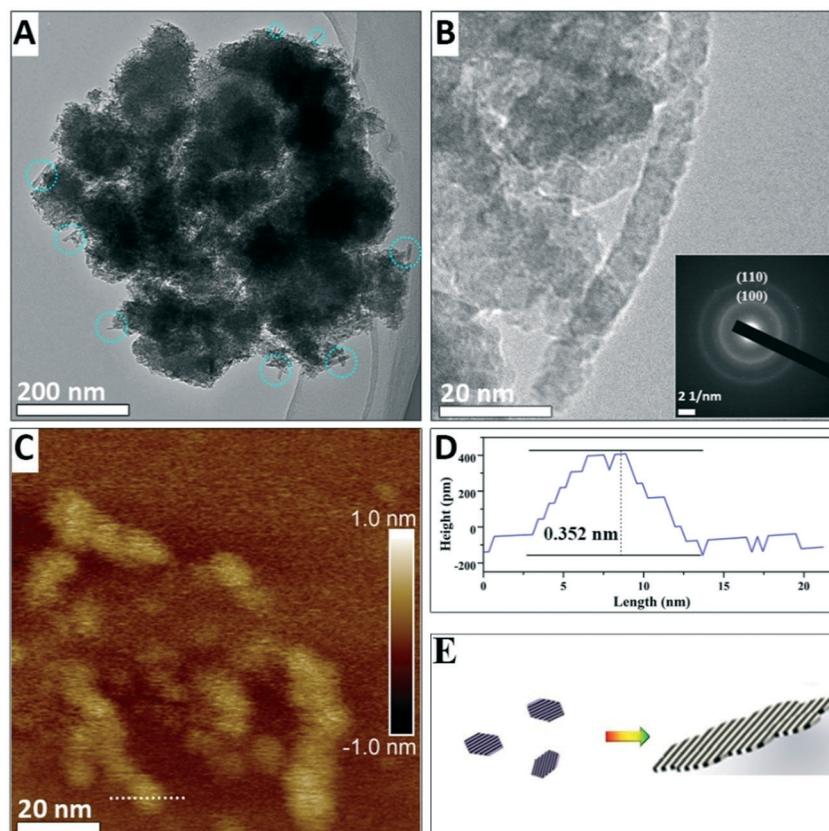
Fig. 2 TEM images of intermediate product of Na100-6 (A and B) and the SAED pattern (B inset). The blue circle in image (A) indicates there are some nanoribbons. AFM image of the intermediate product of Na100-6 (C) and height profile of Na100-6. Profile image (D) corresponds to the trajectory shown in Fig. 2C. (E) Schematic of δ-MnO₂ assembly process.

After the suspension is heated for 14 min, large numbers of nanorods appear, coincident with the disappearance of the δ-MnO₂ nanoflakes (Fig. 4A). The widths of the α-MnO₂ nanorods with better crystallinity, as shown in Fig. 4B, range from 8 to 10 nm. There are two nanorods that assemble at one end to form a continuous lattice along the (110) plane (Fig. 4C). The number of lattice dislocations observed at the attached interface (inset I in Fig. 4C) is higher than that of a single nanorod (inset II in Fig. 4C). The blue square in Fig. 4C indicates that two nanorods separate to form a gap at one end. This process has been extensively reported for the growth of α-MnO₂ nanorods based on the side-to-side OA process.[2,11,20,29,30]

After the final heating stage, the widths and lengths of nanorods increase to ~40 nm and ~400 nm, respectively (Fig. 5A and B). The serrated sides and internal lattice dislocations of nanorods shown in Fig. 5C have almost disappeared owing to the aging process. However, the overlap of individual sheets is still visible at the [001] ends of the rods (Fig. 5C).

Structural evolution

TEM can only observe morphological changes. However, the mechanism based on which δ-MnO₂ transformed to α-MnO₂

at 100 °C for 10 min, and the exact structural changes experienced before transformation were studied using detailed structural characterization. The powder PXRD pattern of the initial δ-MnO₂ shows two broad diffraction peaks at 37° ($d_{(100)}$ = 2.46 Å) and 65° ($d_{(110)}$ = 1.43 Å) (Fig. 6A), which can be attributed to δ-MnO₂ with poor crystallinity, small-sized and randomly stacked [MnO₆] octahedral layers, in good agreement with the SAED pattern shown in the inset of Fig. 1B.[7,23,31] The d-spacing ratio of $d_{(100)}$ to $d_{(110)}$ is 1.73, which indicates a hexagonal layer symmetry.[32–34] The absence of basal (001) and (002) peaks ($d_{(001)}$ = 7.2 Å, $d_{(002)}$ = 3.6 Å) is consistent with TEM and AFM images and further proves that δ-MnO₂ possesses a single [MnO₆] octahedral layer structure (Fig. 1).

Before the suspension was heated at 100 °C for 10 min, only δ-MnO₂ appeared in the PXRD pattern (Fig. 6A–C). The (100) and (110) diffraction peaks of δ-MnO₂ are not sharper than those of the initially formed sample, thus indicating that the sizes of the crystallites did not increase within the a–b planes (Fig. 6C).[18] A detailed inspection of these (100) and (110) peaks suggests a slight structural alteration of δ-MnO₂ evidenced by the appearance of a small shoulder on the high angle side of the (100) peak (Fig. 6C, asterisk symbol). A previous study proposed that this feature could be related to an increased amount of Mn(III) capped on vacancies in the
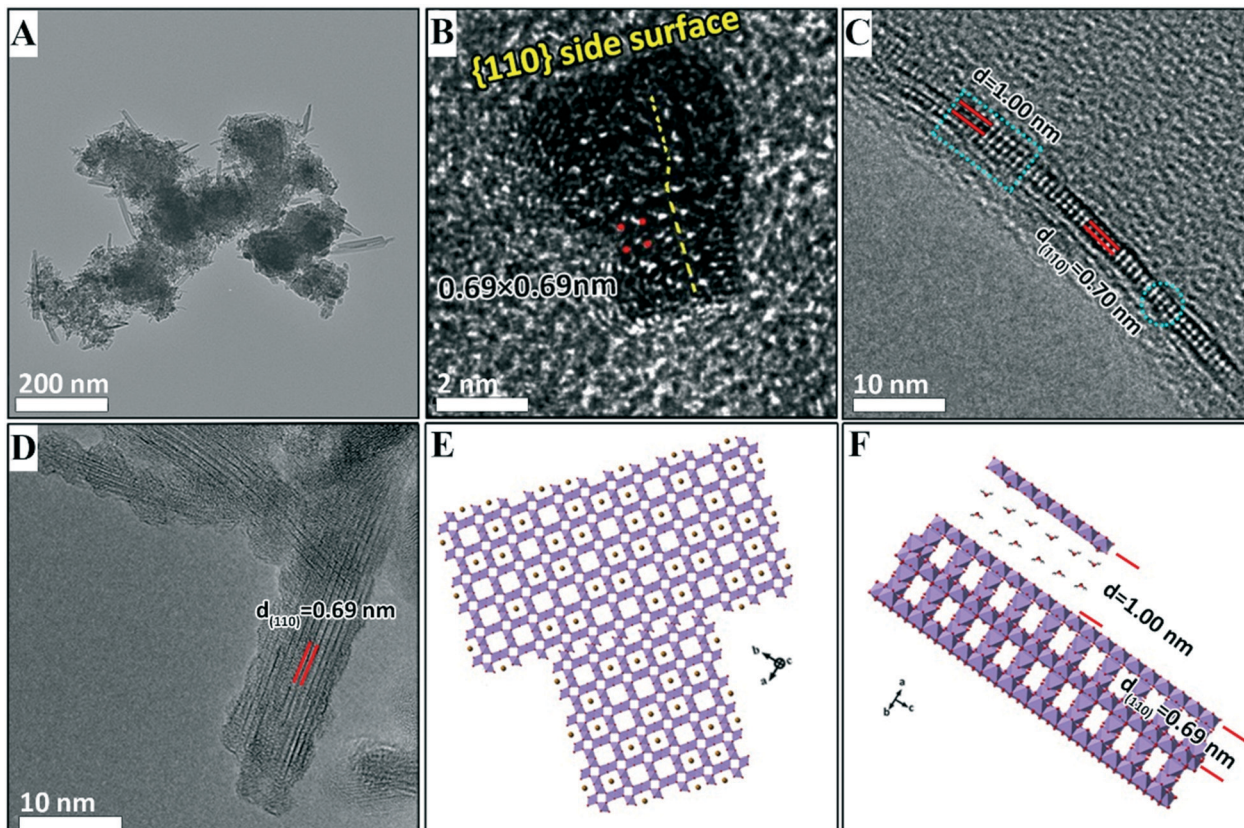
Fig. 3 TEM (A) image of the intermediate Na100-10. (B) High-resolution transmission electron microscopy (HRTEM) image of a primary α-MnO$_2$ nanorod cross-section viewed along the [001] zone axis. (C) HRTEM image of the δ-MnO$_2$ nanoribbon cross-section viewed along the [110] zone axis. The blue circle indicates nanoflakes assembled along the (100) plane. (D) HRTEM image of nanorods. (E and F) Schematics of HRTEM images in (B) and (C), respectively.

[MnO$_6$] octahedral layers.[32] These results suggest that Mn(IV) is being reduced to Mn(III)/Mn(II) and adsorbed on the vacancy sites with increasing reaction times.

After the suspension was heated for 14 min, (110), (200), and (310) α-MnO$_2$ peaks with low intensity appeared (ICDD No. 00-29-1020, $d_{(110)}$ = 0.69 nm, $d_{(200)}$ = 0.48 nm, and $d_{(310)}$ = 0.31 nm), thus indicating that some of the δ-MnO$_2$ was transformed to α-MnO$_2$ during heating in the time interval from 10 min to 14 min (Fig. 6A).[20] The lattice spacing of 0.69 nm (Fig. 3B) for the (110) plane of α-MnO$_2$ can be observed in the PXRD pattern of Na100-10 (Fig. 6B). Therefore, the period along the α-MnO$_2$ (110) plane was formed gradually and is consistent with the formation of α-MnO$_2$ by the addition of the single-layer nanoflakes or the nanoribbons of δ-MnO$_2$. Thickening of the nanoribbons and transformation of structures occurred simultaneously during the 10 min heating period.

Finally, the PXRD half peak width narrowed and the intensities increased gradually during the heating period from 14 to 20 min. This indicated that the crystallite size and crystallinity of α-MnO$_2$ increased (Fig. 6).

During the structural transformation, subtle changes in the PXRD peak may occur owing to the reduction and migration of Mn. Therefore, we speculate that the production and adsorption of Mn(III)/Mn(II) play an important role in the transformation of δ-MnO$_2$ to α-MnO$_2$. The phenomenon

based on which Mn(IV) was reduced to Mn(III)/Mn(II) and adsorbed on the vacancy sites was further confirmed by the results of the pair distribution functions (PDFs). From the peak intensity examination of the PDF, a systematic structural change was observed during the synthetic process (Fig. 6E). From Na100-6 to Na80, the peaks at 2.85 Å and 4.93 Å decreased in intensity. These peaks are attributed to atomic pairs involving the first and second Mn shells within the octahedral layer around specific Mn (Mn$_L$–Mn$_L$1 and Mn$_L$–Mn$_L$2) shells (Fig. S6†).[31,35] By contrast, the correlations at 3.44 Å and 5.28 Å increased in intensity. These increases are attributed to the atomic pairs formed by Mn$_L$ and the Mn interlayer (Mn$_{IL}$) at vacancies belonging to the first (Mn–Mn$_{IL}$1) and second (Mn–Mn$_{IL}$2) shells, respectively. The PDF results also suggest that Mn$_L$ migrates from the layer to the interlayer, above or below the vacancies, to form mono-μ-oxo bridge (with an Mn$_L$–Mn$_{IL}$1 distance of approximately 3.44 Å) [MnO$_6$] octahedra.[35,36] It is likely that these interlayer Mn(III)/Mn(II) octahedra act as templates for the tunnel "walls" during the transformation to α-MnO$_2$.[11,12]

Evolution of the chemical composition

The Mn average oxidation states (AOSs) of the intermediate products provide further quantification of the Mn(III)/Mn(II)
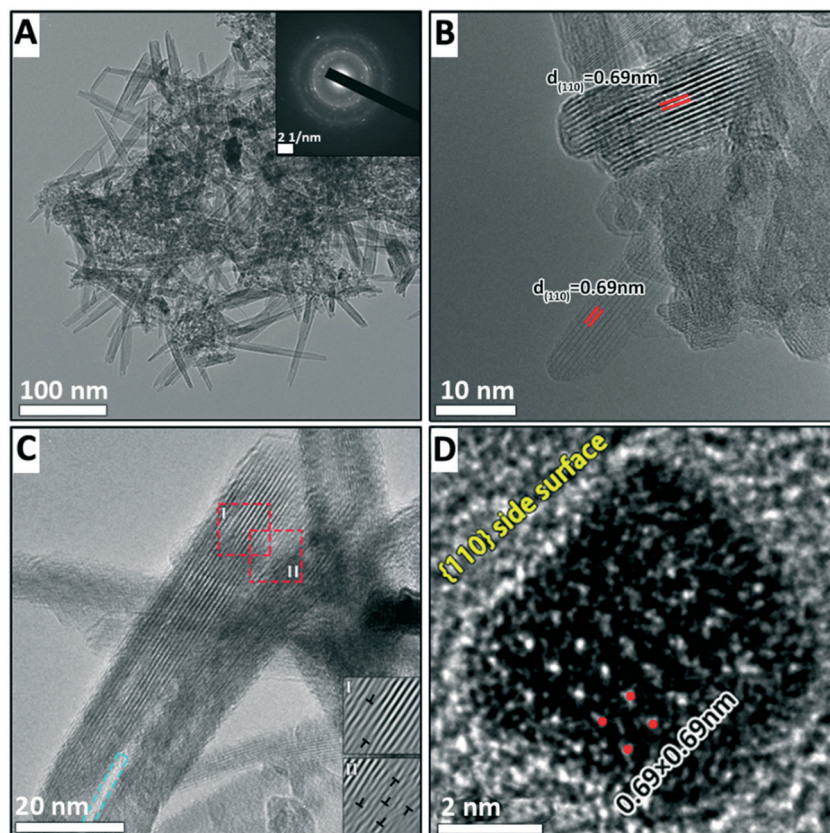
This journal is © The Royal Society of Chemistry 2020

Environ. Sci.: Nano, 2020, **7**, 238–249 | **243**

Fig. 4 TEM (A) image of the intermediate Na100-14. (B) HRTEM image of nanorods. (C) HRTEM images show nanorods assemble along the (110) plane. The blue rectangle indicates that there is a gap between two nanorods. Fourier filtered images of zone I and zone II using red area outlined in (C), highlighting the defects. (D) An image of a nanorod cross section viewed along the [001] zone axis.

production and structural changes of δ-MnO$_2$. The detailed Mn(ɪᴠ), Mn(ɪɪɪ), and Mn(ɪɪ) contents, which were obtained by fitting the XPS narrow scans of the Mn 3s spectra, are listed in Table 1 and Fig. S7.† The AOS of the samples decreased from 3.96 to 3.70 (Table 2, titration data) during the heating period of the suspension (100 °C for 10 min). XPS Mn 3s fitting data show that the percentages of Mn(ɪᴠ) decreased from 92.5% to 84.1%; the percentage of Mn(ɪɪɪ) increased from 6.7% to 12% during this stage. The values of AOS obtained by fitting of XPS Mn2p$_{3/2}$ spectra are systematically lower than those obtained by the titration method, probably owing to the higher content of the lower valence Mn present at the surface.[37–39] Thus, the XPS-derived AOS represents the "surface" Mn AOS, and it is possible that Mn(ɪᴠ) is reduced to Mn(ɪɪɪ)/Mn(ɪɪ) and is adsorbed on the surface of the δ-MnO$_2$ nanoparticles. Despite the discrepancy between the absolute AOS values, we obtained similar trends in the evolution of AOS with the reaction derived from the two methods.

Previous studies have shown that structural Mn(ɪɪɪ) is critical to the transformation of layer-structured Mn oxides into tunneled ones.[40] However, the mechanism by which Mn(ɪɪɪ) was reduced from Mn(ɪᴠ) in the initial δ-MnO$_2$ is still an open question. As described above, some of the octahedral Mn(ɪᴠ) was initially reduced to Mn(ɪɪ), and part of it was subsequently transformed to Mn(ɪɪɪ). Given that apart from O$_2$–H$_2$O

(H$^+$), no other reductant existed during the transformation of δ-MnO$_2$ to α-MnO$_2$, there are two possible pathways to describe the reduction of Mn(ɪᴠ).

One way is that the MnO$_2$ is reduced by H$_2$O at ~100 °C and pH < 1, according to eqn (3).[41]

$$MnO_2 + 2H^+ \rightarrow Mn^{2+} + H2O + \frac{1}{2}O_2 \qquad (3)$$
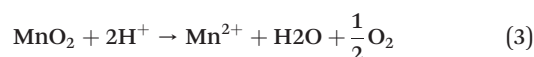
Depending on the pH, the Mn(ɪɪ) cations originating from oxidation of lattice O^{2-} under acidic conditions may attach above/below the layer vacancies.[11,41,42] The PXRD pattern of NaMix in Fig. 6 shows that the crystallinity of δ-MnO$_2$ was poor (*i.e.*, a small crystallite size), thus indicating a large surface area, which favors eqn (3).

A second possible pathway for the reduction of Mn(ɪᴠ) involves the poorly crystalline δ-MnO$_2$ with mixed-Mn valences (ɪɪ, ɪɪɪ, and ɪᴠ) and the release of structural oxygen, according to eqn (4).[43,44]

$$\left[-Mn(\text{ɪᴠ})-O^{2-}-Mn(\text{ɪᴠ})-\right] \rightarrow \left[-Mn(\text{ɪɪɪ})-\square-Mn(\text{ɪɪɪ})-\right] + \frac{1}{2}O_2 \qquad (4)$$
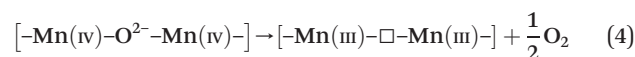
The XPS fitting results of O1s are listed in Table 1. There are three species of oxygen in Mn oxides, lattice oxygen (O^{2-}),
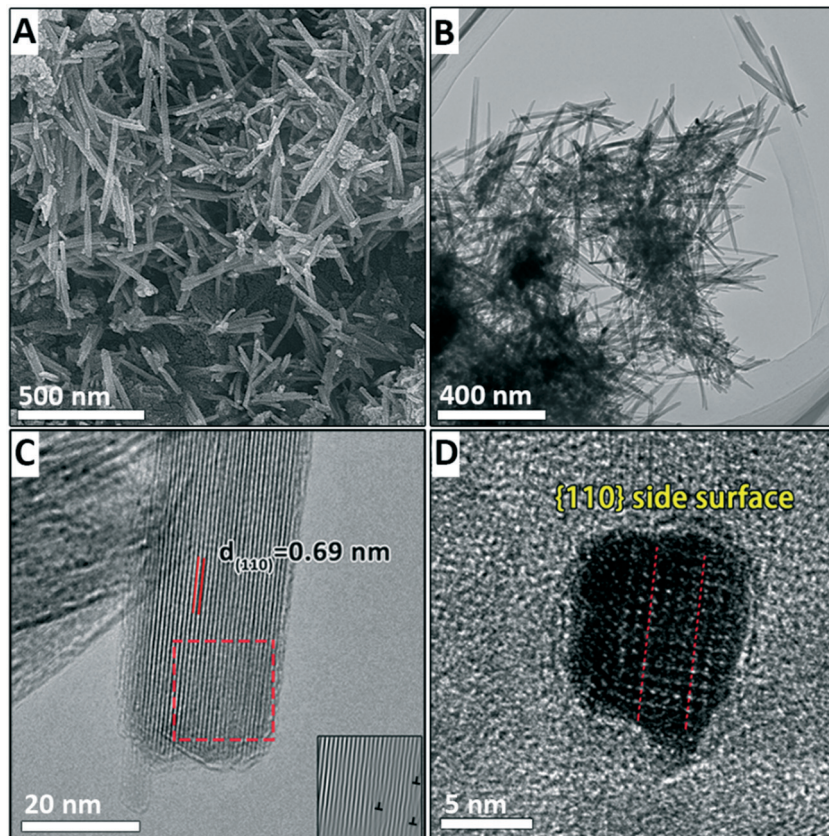
Fig. 5 FESEM image of product of Na80 (A), TEM image (B) and HRTEM image (C) showing α-MnO$_2$ nanoparticles. Fourier filtered image (C inset) using red area outlined in (C), highlighting the defects. (D) An image of a nanorod cross section viewed along the [001] zone axis.

hydroxide oxygen (–OH), and oxygen in molecular water. Among the three species of oxides, O^{2-} decreased from 69.9% to 56.2%, and –OH increased from 18.1% to 26.3% during the heating of the suspension during the first 10 min. The large amount of lost O^{2-} was not proportional to the formed –OH. It is interesting that this great loss of O^{2-} is consistent with the creation of O vacancies in δ-MnO$_2$, as proposed above (eqn (4)). The observed increase of the O1s peak at 532.4 eV in the XPS spectra is induced by the formation of oxygen vacancies (Fig. S8†).[45–48] Furthermore, the increase in the content of Na$^+$ and Mn(III) (longer Mn–O bond), and the poor crystallinity could facilitate the formation of oxygen vacancies (Tables 1 and 2), which promote the production of Mn(III) and the transformation of a 2D layer structure into a one-dimensional (1D) tunnel structure.[41,49,50]

After forming the tunnel structure, the intensities of the O1s XPS peaks at 532.4 eV were maximized, and the AOS of δ-MnO$_2$ reached a minimum during the 10 min heating period. The reactions described in eqn (3) and (4) became less favorable owing to the formation of a more stable structure of α-MnO$_2$, and the percentages of Mn(III) and Mn(II) decreased gradually (Table 1). Additionally, the decrease of the O1s XPS peak at 532.4 eV was induced by the reduction of oxygen vacancies (Fig. S8†). This indicated that dissolved oxygen generated by the reactions of eqn (3) and (4) could refill the oxygen vacancies and oxidize Mn(III)/Mn(II) back to Mn(IV)

after the formation of α-MnO$_2$, which caused the increase of AOS from 3.70 to 3.96 (Table 2).

Coupled morphological and structural evolution

Based on the above analyses, the coupled evolutions of structure (Fig. 6) and morphology (Fig. S9†) during the formation of α-MnO$_2$ are illustrated in Fig. 7. Firstly, MnO$_4^-$ is reduced by Mn(II) to produce primary nanoflakes of δ-MnO$_2$ with poor crystallinity and with sizes in the range of 2–4 nm. Upon increasing the heating time, nanoflakes aggregate serially to form nanoribbons. Secondly, the nanoribbons stack with each other to form primary nanorods, which initiate the conversion of δ-MnO$_2$ into α-MnO$_2$. Finally, the primary nanorods assemble along the (110) and (001) planes by side-to-side and end-to-end OA, respectively.

The structure of δ-MnO$_2$ produced in the initial crystallization stage does not meet the necessary conditions, i.e., increased proportion of Mn(III)/Mn(II) above or below the layer vacancies, for its conversion to α-MnO$_2$. Although δ-MnO$_2$ did not convert to α-MnO$_2$ before it was heated (for a period of 10 min), the lower pH of 0.86 was favorable for edge-to-edge aggregation along the (100) plane.[7] The initially formed nanoribbons that were formed by the nanoflakes and were attached to each other have many lattice dislocations at the grain boundaries (Fig. 2B and 3C) and promote the
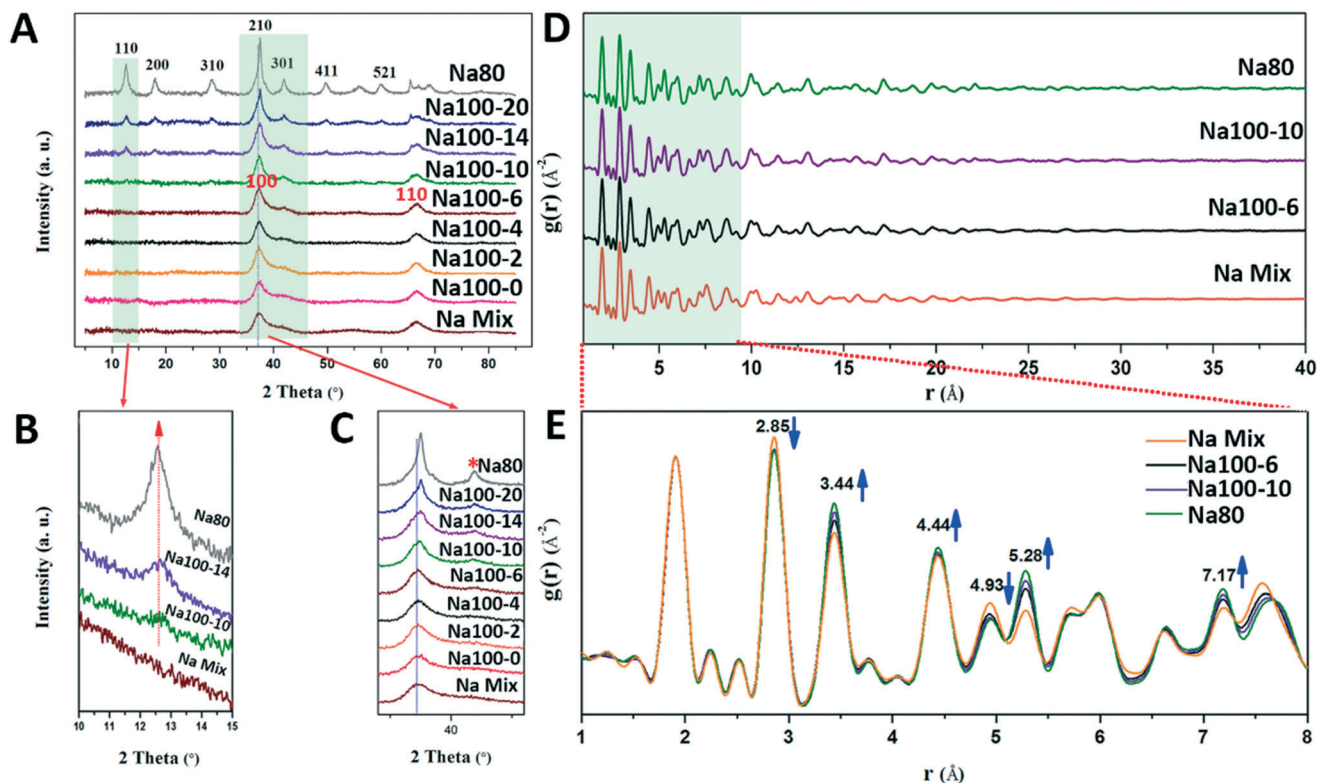
This journal is © The Royal Society of Chemistry 2020

Environ. Sci.: Nano, 2020, 7, 238–249 | 245

Fig. 6 (A) PXRD patterns of intermediate products at different intervals of Na^+ stabilized α-MnO_2 formation and crystal growth. Red indicates the crystal surface of δ-MnO_2, black indicates the crystal surface of α-MnO_2 (B and C). The green zone is shown in a magnified view. The asterisk in (C) is a sign of shoulder peaks. (E and D) Pair distribution functions [$G(r)s$] of intermediate products at different time intervals of Na^+ stabilized α-MnO_2 formation and crystal growth.

generation of oxygen vacancies.[51] The Mn(III) moieties were generated based on the generation of oxygen.

Subsequently, structural adjustments occur through the production and migration of Mn(III) in the δ-MnO_2 nanoflakes and nanoribbons. Recently, Ling *et al.* showed that the amount of Mn(III) has an impact on the structure of δ-MnO_2.[52] Furthermore, Cui *et al.* and Yuan *et al.* revealed that the interlayer Mn(III) plays an important role in building a tunnel structure during the conversion of LMOs (buserite) to TMOs (3 × 3 todorokite).[21,40] The amount of Mn(IV)/(III) for the ideal transition state structure can be obtained, as shown in Fig. S10;† *i.e.*, the required interlayer Mn(III) content is 30% of the total Mn to assemble into the α-MnO_2 structure. This agrees very well with our experimental observations. The AOS of the production of onset of transformation into Na^+-

stabilized α-MnO_2 and K^+-stabilized α-MnO_2 were 3.70 and 3.74 with Mn(III) concentration about 30% and 26%, respectively. Sufficient Mn(III) was required for the formation of the tunnel "walls" to support the transformation, and for the provision of sufficient hydrogen bonding. Indeed, [Mn(III)O_6] octahedra are distorted by the Jahn–Teller effect, and bonding distortion within the octahedral layer is relieved when Mn(III) migrates from layers to locations above and below the vacancies (Fig. 7, step 1).[11] These [Mn(III)O_6] octahedra include three unsaturated oxygen molecules that were combined with H^+ to form –OH. When the amount of –OH was large enough, a network of hydrogen bonds formed between the [Mn(III)O_6] octahedra of adjacent nanosheets and nanoflakes (Fig. 7, step 2, 3). These [Mn(III)O_6] octahedra dehydrated *via* a condensation reaction and formed the tunnel "walls." Therefore, the number of –OH moieties is expected to be maximized at the initial stage of the transformation, and to decrease during the subsequent transformation stages. These nanoribbons and nanoflakes attach along the (001) plane of δ-MnO_2 to form primary α-MnO_2 nanorods based on face-to-face OA (Fig. 7, step 4). This is the process of structural evolution used to promote the transformation of morphological and crystal phase changes.

To confirm this formation mechanism in α-MnO_2 with different tunnel cations, K^+-stabilized α-MnO_2 was synthesized with similar procedures, whereby only $NaMnO_4$ was replaced

Table 1 Compositions of Mn and O species derived from fittings of Mn (3s) and O (1s)

Samples	Mn			O		
	Mn(III) (±0.003)	Mn(II) (±0.001)	Mn(IV) (±0.003)	O^{2-}	OH^-	H_2O
NaMix	0.067	0.008	0.925	0.699	0.181	0.120
Na100-4	0.100	0.001	0.889	0.621	0.224	0.155
Na100-10	0.120	0.039	0.841	0.562	0.263	0.175
Na100-14	0.091	0.029	0.880	0.610	0.229	0.161
Na80	0.048	0.00	0.931	0.685	0.192	0.123

246 | *Environ. Sci.: Nano*, 2020, **7**, 238–249

This journal is © The Royal Society of Chemistry 2020

Table 2 Na$^+$ content, average oxidation state (AOS) of Mn in intermediate products at various time intervals during Na$^+$-stabilized α-MnO$_2$ formation obtained from titration and fittings of Mn 2p$_{3/2}$ and Mn 3s

Samples	XPS (Mn 2p$_{3/2}$)	XPS (Mn 3s)	Titration	Chemical composition
NaMix	3.81	3.92	3.96 ± 0.01	Na$_{0.029}$MnO$_{1.994}$·0.54H$_2$O
Na100-0	—	—	3.96 ± 0.02	Na$_{0.039}$MnO$_{1.999}$·0.63H$_2$O
Na100-4	3.78	3.87	3.86 ± 0.02	Na$_{0.055}$MnO$_{1.957}$·0.77H$_2$O
Na100-6	—	—	3.75 ± 0.03	—
Na100-10	3.76	3.79	3.70 ± 0.01	Na$_{0.090}$MnO$_{1.895}$·0.86H$_2$O
Na100-14	3.78	3.85	3.78 ± 0.04	Na$_{0.067}$MnO$_{1.923}$·0.57H$_2$O
Na100-16	—	—	3.95 ± 0.02	Na$_{0.061}$MnO$_{2.006}$·0.67H$_2$O
Na100-18	—	—	3.98 ± 0.03	Na$_{0.057}$MnO$_{2.018}$·0.62H$_2$O
Na100-20	—	—	3.96 ± 0.01	Na$_{0.048}$MnO$_{2.004}$·0.53H$_2$O
Na80	3.83	3.91	3.92 ± 0.02	Na$_{0.032}$MnO$_{1.976}$·0.67H$_2$O
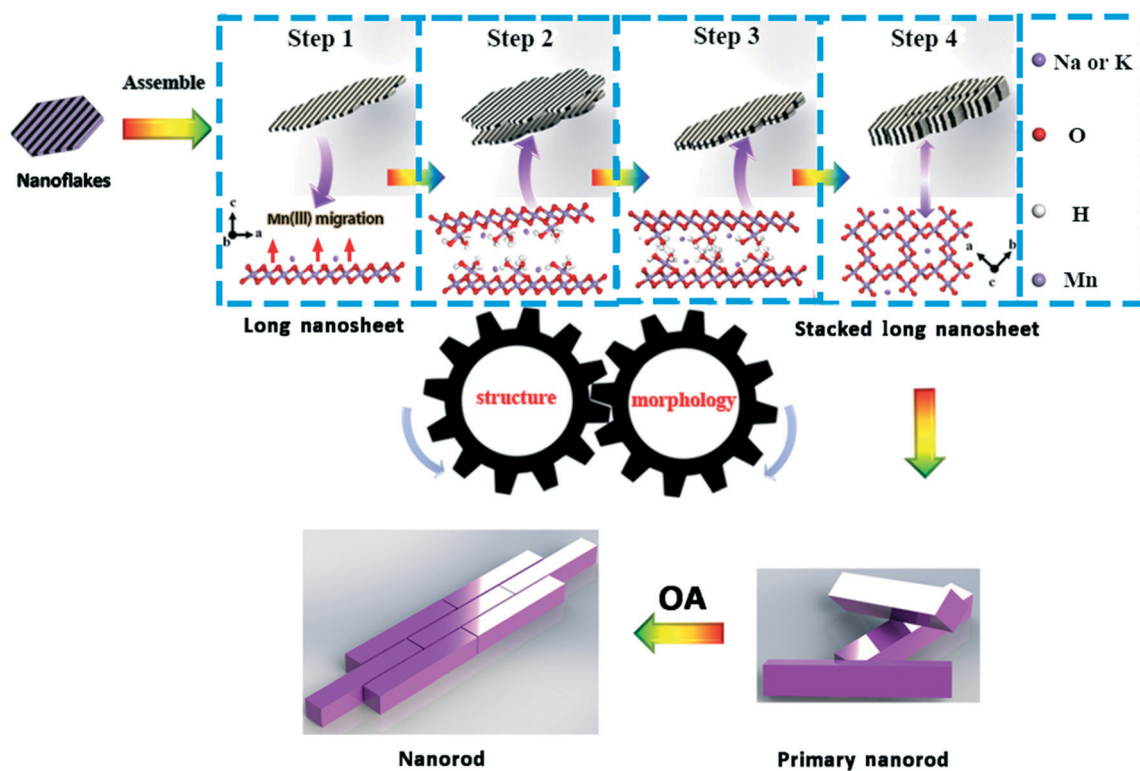
Fig. 7 Proposed processes of assembly of nanoparticles and morphological evolution with time during the crystal growth of α-MnO$_2$ via a staged OA process. The schematic in the blue square illustrates the structural changes and morphological evolutions during the δ-MnO$_2$ transformation to α-MnO$_2$.

by KMnO$_4$. During the synthesis of K$^+$-stabilized α-MnO$_2$, all the trends of the structural evolution were consistent with those of Na$^+$-stabilized α-MnO$_2$ (Fig. S11 and Tables S1 and S2†). It is suggested that the different tunnel cations of α-MnO$_2$ experienced a similar OA formation process. The δ-MnO$_2$ molecules were converted to α-MnO$_2$ using heating at 100 °C for a 2 min period. The PXRD analysis (Fig. S11†) indicated that the conversion rate of K$^+$-stabilized δ-MnO$_2$ was much faster than that of Na$^+$-stabilized δ-MnO$_2$. The structure of K$^+$-stabilized α-MnO$_2$ was stable when the suspension was aged for 24 h, while previous reports indicated that the stable (100) surface of nanorods could be formed during this stage.[20] However, when the Na$^+$-stabilized α-MnO$_2$ was continually aged for 24 h, the PXRD patterns of the samples yielded a new peak, d_{hkl} = 0.4 nm, of γ-MnO$_2$ with a 1 × 2 tunnel structure (Fig. S12†) because of the small amount of Na$^+$ used (3.24 ± 0.09% in Table 2) in the tunnel to stabilize the Na$^+$-stabilized α-MnO$_2$.[50] These results indicate that the K$^+$ adsorbed on δ-MnO$_2$ not only accelerated the production and migration of Mn(III), but also promoted the structural conversion and stability of the produced α-MnO$_2$. This finding agrees well with previous reports that indicated that the K$^+$ ions, whose size (~0.138 nm) facilitated trapping of the 2 × 2 tunnel size (~0.46 nm), played important roles in the templating and stabilization of the tunneled framework.[53]

This journal is © The Royal Society of Chemistry 2020

Environ. Sci.: Nano, 2020, **7**, 238–249 | **247**

Another difference between the K$^+$-stabilized α-MnO$_2$ and Na$^+$-stabilized α-MnO$_2$ is the dominant side crystallographic face of the products. In this study, the cutting of the nanorods of Na$^+$-stabilized α-MnO$_2$ along the (001) plane at different stages shows that the side planes of the nanorods still correspond with the (110) plane (Fig. 5D and S13†). This is in part attributed to the fact that the open tunnel structure is formed more easily during the assembly process, and the morphology can be better captured during a slower Na synthesis. The nanorods of Na$^+$ stabilized α-MnO$_2$ with the exposed (110) lateral facets may be the intermediate products that can be stably present over a period of time due to a slow reaction rate. In the presence of K$^+$, the side faces of the nanorods become four (100) faces with a lower energy of 0.44 J m^{-2} compared to the (110) surface energy of 0.74 J m^{-2} through a dissolution–recrystallization reaction (Fig. S13†).[19] K$^+$ stabilized α-MnO$_2$ is formed more than 5 times faster than Na$^+$ stabilized α-MnO$_2$ during the same synthesis period, and it has a longer aging time, so that the K$^+$ stabilized α-MnO$_2$ nanorods tend to expose stable (100) edge surfaces by the dissolution–recrystallization driven by the surface energy difference. Therefore, α-MnO$_2$ nanorods with different exposed lattice faces can be obtained during the synthesis according to the specific application. The Na$^+$-stabilized α-MnO$_2$ is more suitable for producing nanorods with four (110) lateral faces, which likely reduce the distance and energy barrier for ion diffusion, and improve the rate performance of α-MnO$_2$ in various applications, such as rechargeable battery electrodes, supercapacitors, and Li–O$_2$ battery catalysts.[17,54–59] Conversely, the K$^+$-stabilized α-MnO$_2$ is more suitable for producing long nanowires because of its stable tunnel structure with the support of K$^+$.

Although this study is not exhaustive, it does highlight an important area for further studies on the morphological and structural interactions. Indeed, future studies could evaluate K$^+$ ion template effects on the migration of Mn(III) into tunnel "walls" and the changes in the reactivities of the products that are formed in different stages.

Conclusion

Na$^+$-Stabilized tunnel structured α-MnO$_2$ nanorods were found to assemble via a staged OA growth process. The coupled evolution of structure and morphology during the entire process has been explored.

Firstly, the δ-MnO$_2$ nanoflakes, which possessed poorly crystalline forms, aggregated along the (110) surface plane to form δ-MnO$_2$ nanoribbons via the edge-to-edge aggregation mechanism. Meanwhile, the Mn(IV) ions in the [MnO$_6$] octahedral layer of δ-MnO$_2$ were reduced to Mn(III) by water, and then migrated above and below the vacancies. Secondly, the morphology and structure of δ-MnO$_2$ evolved simultaneously. Mn(III), whose amount increased gradually, built up tunnel walls and triggered the conversion of the 2D layer structure to the 1D tunnel structure. A dynamic network of hydrogen bonds between the –OH groups, which were combined with

Mn(III) of adjacent nanoribbons, was present as a mode of bonding to fabricate the tunnel structure. Therefore, adjacent nanoribbons aggregated and formed α-MnO$_2$ primary nanorods based on the face-to-face OA mechanism. Thirdly, primary nanorods assembled with each other to form longer and wider nanorods based on respective end-to-end and side-to-side OA mechanisms. The defects that were formed by the assembly process were constantly smoothed via dissolution–recrystallization processes throughout the entire reaction. This work has filled the gap regarding the initial stage of 1D tunnel-structured α-MnO$_2$ formation under natural conditions. Meanwhile, it also provided greater fundamental understanding of the relationship between the structure and morphological transformation during the crystal growth process.

Conflicts of interest

There are no conflicts to declare.

Acknowledgements

References

1 L. Penn and J. F. Banfield, *Science*, 1998, **281**, 969–971.

2 J. J. De Yoreo, P. U. Gilbert, N. A. Sommerdijk, R. L. Penn, S. Whitelam, D. Joester, H. Zhang, J. D. Rimer, A. Navrotsky and J. F. Banfield, *Science*, 2015, **349**, aaa6760.

3 J. Zhang, F. Huang and Z. Lin, *Nanoscale*, 2010, **2**, 18–34.

4 X. Liang, Z. Zhao, M. Zhu, F. Liu, L. Wang, H. Yin, G. Qiu, F. Cao, X. Liu and X. Feng, *Environ. Sci.: Nano*, 2017, **4**, 1656–1669.

5 H. Zhao, M. Zhu, W. Li, E. J. Elzinga, M. Villalobos, F. Liu, J. Zhang, X. Feng and D. L. Sparks, *Environ. Sci. Technol.*, 2016, **50**, 1750–1758.

6 Q. Wang, X. Liao, W. Xu, R. Yang, K. J. Livi and M. Zhu, *Inorg. Chem.*, 2016, **55**, 10248–10258.

7 F. F. Marafatto, B. Lanson and J. Peña, *Environ. Sci.: Nano*, 2018, **5**, 497–508.

8 A. L. Atkins, S. Shaw and C. L. Peacock, *Geochim. Cosmochim. Acta*, 2014, **144**, 109–125.

9 S. L. Suib, *Acc. Chem. Res.*, 2008, **41**, 479–487.

10 S. Dharmarathna, C. K. King'Ondu, W. Pedrick, L. Pahalagedara and S. L. Suib, *Chem. Mater.*, 2012, **24**, 705–712.

11 S. Grangeon, A. Fernandezmartinez, F. Warmont, A. Gloter, N. Marty, A. Poulain and B. Lanson, *Geochem. Trans.*, 2015, **16**, 12.

248 | *Environ. Sci.: Nano*, 2020, **7**, 238–249

This journal is © The Royal Society of Chemistry 2020

12 S. Grangeon, B. Lanson and M. Lanson, *Acta Crystallogr., Sect. B: Struct. Sci., Cryst. Eng. Mater.*, 2014, **70**, 828–838.

13 Y. F. Yuan, C. Liu, B. W. Byles, W. Yao, B. Song, M. Cheng, Z. Huang, K. Amine, E. Pomerantseva, R. Shahbazian-Yassar and J. Lu, *Joule*, 2019, **3**, 1–14.

14 J. Liu, V. Makwana, J. Cai, S. L. Suib and M. Aindow, *J. Phys. Chem. B*, 2003, **107**, 9185–9194.

15 S. Parc, D. Nahon, Y. Tardy and P. Bieillard, *Am. Mineral.*, 1989, **74**, 466–475.

16 J. Ostwald, *Econ. Geol.*, 1992, **87**, 1237–1252.

17 P. M. Vasconcelos, P. R. Renne, G. H. Brimhall and T. A. Becker, *Geochim. Cosmochim. Acta*, 1994, **58**, 1635–1665.

18 T. T. Truong, Y. Liu, Y. Ren, L. Trahey and Y. Sun, *ACS Nano*, 2012, **6**, 8067–8077.

19 K. Li, J. Chen, Y. Peng, W. Lin, T. Yan and J. Li, *J. Mater. Chem. A*, 2017, **5**, 20911–20921.

20 Y. Yuan, S. M. Wood, K. He, W. Yao, D. Tompsett, J. Lu, A. Nie, M. S. Islam and S. Santhanagopalan, *ACS Nano*, 2016, **10**, 539–548.

21 Y. F. Yuan, K. He, B. W. Byles, C. Liu, K. Amine, J. Lu, E. Pomerantseva and R. Shahbazian-Yassar, *Chem*, 2019, **5**, 1793–1805.

22 S. Grangeon, B. Lanson and M. Lanson, *Acta Crystallogr., Sect. B: Struct. Sci., Cryst. Eng. Mater.*, 2014, **70**, 828–838.

23 D. Portehault, S. Cassaignon, E. Baudrin and J. P. Jolivet, *J. Mater. Chem.*, 2009, **19**, 2407–2416.

24 D. Portehault, S. Cassaignon, E. Baudrin and J. Jolivet, *Chem. Mater.*, 2007, **19**, 5410–5417.

25 D. Zhai, B. Li, C. Xu, H. Du, Y. He, C. Wei and F. Kang, *J. Power Sources*, 2011, **196**, 7860–7867.

26 N. Kijima, H. Yasuda, T. Sato and Y. Yoshimura, *J. Solid State Chem.*, 2001, **159**, 94–102.

27 E. S. Iton, J. E. Post, P. J. Heavey, F. T. Ling and S. N. Kerisit, *Appl. Surf. Sci.*, 2016, **366**, 475–485.

28 R. M. Mckenzie, *Mineral. Mag.*, 1971, **38**, 493–502.

29 H. Zhang, J. J. De Yoreo and J. F. Banfield, *ACS Nano*, 2014, **8**, 6526–6530.

30 X. Zhang, Y. He, M. L. Sushko, J. Liu, L. Luo, J. J. De Yoreo, S. X. Mao, C. M. Wang and K. M. Rosso, *Science*, 2017, **356**, 434–437.

31 M. Villalobos, B. Toner, J. Bargar and G. Sposito, *Geochim. Cosmochim. Acta*, 2003, **67**, 2649–2662.

32 V. A. Drits, B. Lanson and A. C. Gaillot, *Am. Mineral.*, 2007, **92**, 771–788.

33 S. Grangeon, B. Lanson, N. Miyata, Y. Tani and A. Manceau, *Am. Mineral.*, 2010, **95**, 1608–1616.

34 H. Yin, W. Tan, L. Zheng, H. Cui, G. Qiu, F. Liu and X. Feng, *Geochim. Cosmochim. Acta*, 2012, **93**, 47–62.

35 A. Manceau, M. A. Marcus, S. Grangeon, M. Lanson, B. Lanson, A. C. Gaillot, S. Skanthakumar and L. Soderholm, *J. Appl. Crystallogr.*, 2013, **46**, 193–209.

36 V. Petkov, Y. Ren, I. Saratovsky, P. Pastén, S. J. Gurr, M. A. Hayward, K. R. Poeppelmeier and J. F. Gaillard, *ACS Nano*, 2009, **3**, 441–445.

37 I. Zaharieva, P. Chernev, M. Risch, K. Klingan, M. Kohlhoff, A. Fischer and H. Dau, *Energy Environ. Sci.*, 2012, **5**, 7081–7089.

38 H. Yin, F. Liu, X. Feng, T. Hu, L. Zheng, G. Qiu, L. K. Koopal and W. Tan, *Geochim. Cosmochim. Acta*, 2013, **117**, 1–15.

39 H. Yin, X. Feng, G. Qiu, W. Tan and F. Liu, *J. Hazard. Mater.*, 2011, **188**, 341–349.

40 H. Cui, X. Liu, W. Tan, X. Feng, F. Liu and H. Daniel Ruan, *Clays Clay Miner.*, 2008, **56**, 397–403.

41 A. T. Stone, *Environ. Sci. Technol.*, 1987, **2**, 979–988.

42 E. B. Godunov, A. D. Izotov and I. G. Gorichev, *Inorg. Mater.*, 2018, **54**, 66–71.

43 E. B. Godunov, I. V. Artamonova, I. G. Gorichev and Y. A. Lainer, *Russ. Metall.*, 2012, **1**, 39–44.

44 J. Hou, Y. Li, L. Liu, L. Ren and X. Zhao, *J. Mater. Chem. A*, 2013, **1**, 6736–6741.

45 M. Xing, J. Zhang, F. Chen and B. Tian, *Chem. Commun.*, 2011, **47**, 4947–4949.

46 K. Wang, Y. Chang, L. Lv and Y. Long, *Appl. Surf. Sci.*, 2015, **351**, 164–168.

47 Y. Sun, X. Yan, X. Zheng, Y. Liu, Y. Shen and Y. Zhang, *Nano Res.*, 2016, **9**, 1116–1124.

48 J. P. Holgado, G. Munuera, J. P. Espinós and A. R. González-Elipe, *Appl. Surf. Sci.*, 2000, **158**, 164–171.

49 X. Li, J. Ma, L. Yang, G. He, C. Zhang, R. Zhang and H. He, *Environ. Sci. Technol.*, 2018, **52**, 12685–12696.

50 G. Zhang, W. Dong, X. Huang and J. Zou, *Catal. Commun.*, 2017, **89**, 117–120.

51 J. A. Dawson and I. Tanaka, *ACS Appl. Mater. Interfaces*, 2014, **6**, 17776–17784.

52 F. T. Ling, J. E. Post, P. J. Heaney and E. S. Ilton, *Chem. Geol.*, 2018, **479**, 216–227.

53 J. A. Dawson and I. Tanaka, *ACS Appl. Mater. Interfaces*, 2014, **6**, 17776–17784.

54 C. Wei, C. Xu, B. Li, H. Du, D. Nan and F. Kang, *J. Power Sources*, 2013, **225**, 226–230.

55 L. Li, C. Nan, J. Lu, Q. Peng and Y. Li, *Chem. Commun.*, 2012, **48**, 6945–6947.

56 T. S. Arthur, R. Zhang, L. Chen, P. A. Glans, X. Fan, J. Guo and F. Mizuno, *ACS Appl. Mater. Interfaces*, 2014, **6**, 7004–7008.

57 G. S. Hutchings, J. Rosen, D. Smiley, G. R. Goward, P. G. Bruce and F. Jiao, *J. Phys. Chem. C*, 2014, **118**, 12617–12624.

58 Y. Qin, J. Lu, P. Du, Z. Chen, Y. Ren, T. Wu, J. T. Miller, J. Wen, D. J. Miller and Z. Zhang, *Energy Environ. Sci.*, 2013, **6**, 519–531.

59 W. Xiao, H. Xia, J. Y. H. Fuh and L. Lu, *J. Power Sources*, 2009, **193**, 935–938.

This journal is © The Royal Society of Chemistry 2020

Environ. Sci.: Nano, 2020, **7**, 238–249 | **249**

Coupled Morphological and Structural Evolution of δ-MnO$_2$ to α-MnO$_2$ through Multistage Oriented Assembly Processes: the Role of Mn(III)

Xinran Liang,[a, b] Jeffrey E. Post,[c] Bruno Lanson,[d] Xiaoming Wang,[a] Mengqiang Zhu,[e] Fan Liu,[a] Wenfeng Tan,[a] Xionghan Feng,[a*] Guomin Zhu,[b] Xin Zhang,[b] James. J. De Yoreo[b]

a Key Laboratory of Arable Land Conservation (Middle and Lower Reaches of Yangtse River), Ministry of Agriculture, College of Resources and Environment, Huazhong Agricultural University, Wuhan 430070, China

b Physical Sciences Division, Pacific Northwest National Laboratory, Richland, WA 99352 United States

c Department of Mineral Sciences, Smithsonian Institution, Washington, DC 20013, USA

d University of Grenoble Alpes, CNRS, ISTerre, F-38000 Grenoble, France

e Department of Ecosystem Science and Management, University of Wyoming, Laramie, WY, 82071, United States.

Supporting Figures
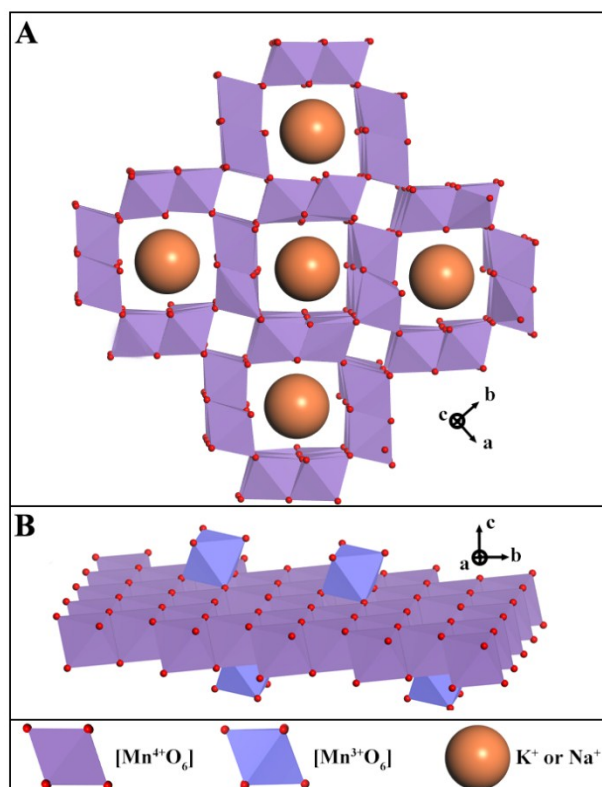
Figure S1. (A) α-MnO$_2$ [MnO$_6$] octahedra tunnel structure model; (B) δ-MnO$_2$ [MnO$_6$] octahedra layer structure model.
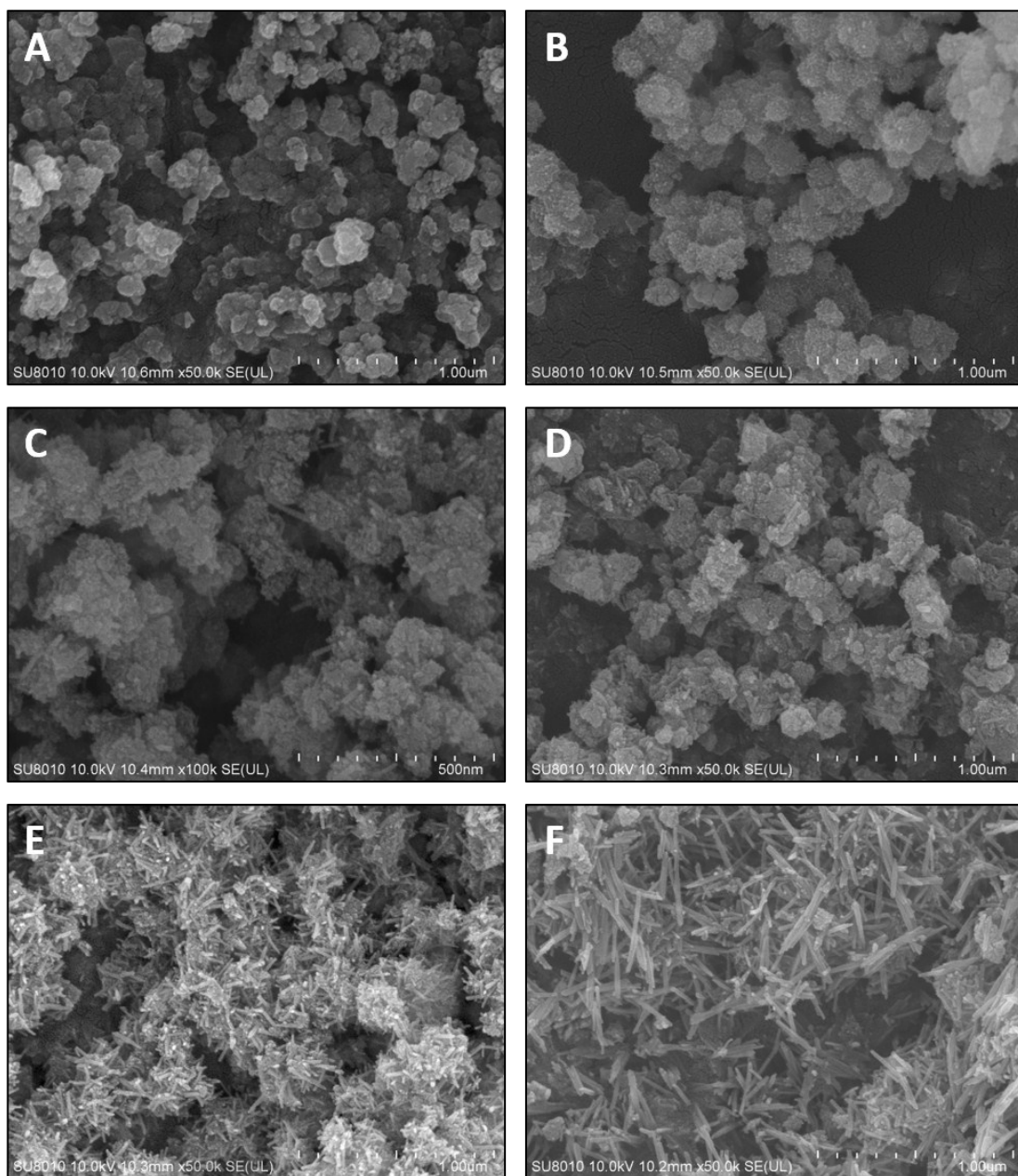
Figure S2. FESEM of intermediate product of (A) NaMix, (B) Na100-2, (C) Na100-6, (D) Na100-10, (E) Na 100-14 and (F) Na80.
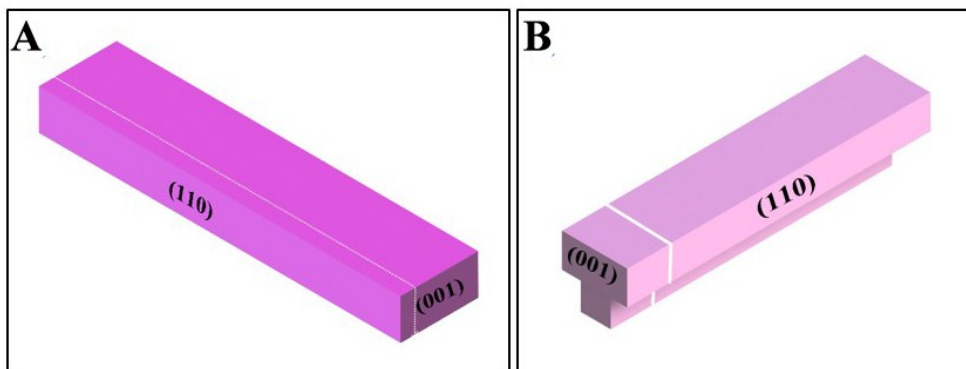
Figure S3. (A) The long nanosheets are cut along (001) plane, (B) The nanorods are cut along (001) plane.
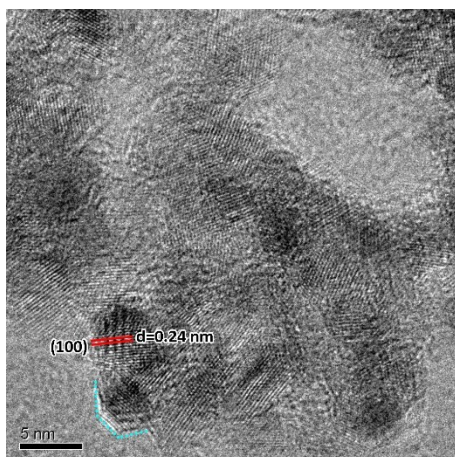
Figure S4. HRTEM image of the initial NaMix indicate the size about the edge of primary nanoflakes to be 3-4 nm
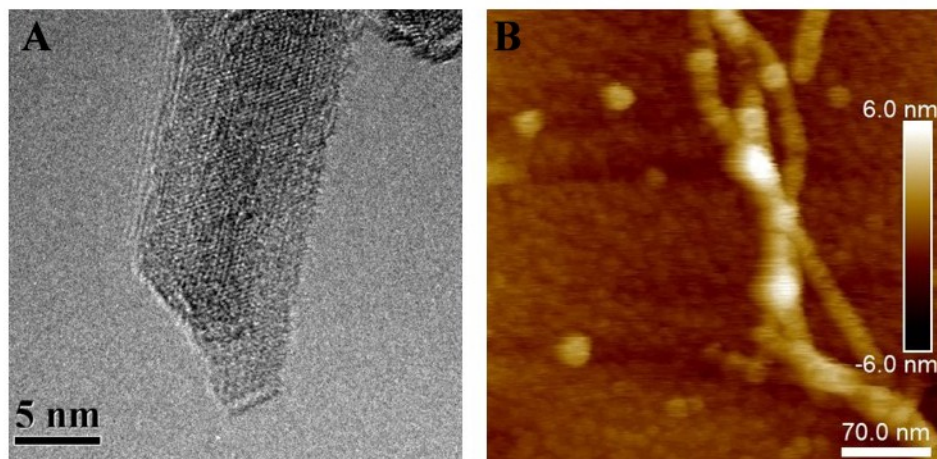
Figure S5. (A) HRTEM image of the intermediate Na100-10 indicate two long nanosheets stack and thicken. (B) AFM image of the intermediate Na100-10 indicate the nanoflakes stack on the nanoribbon.
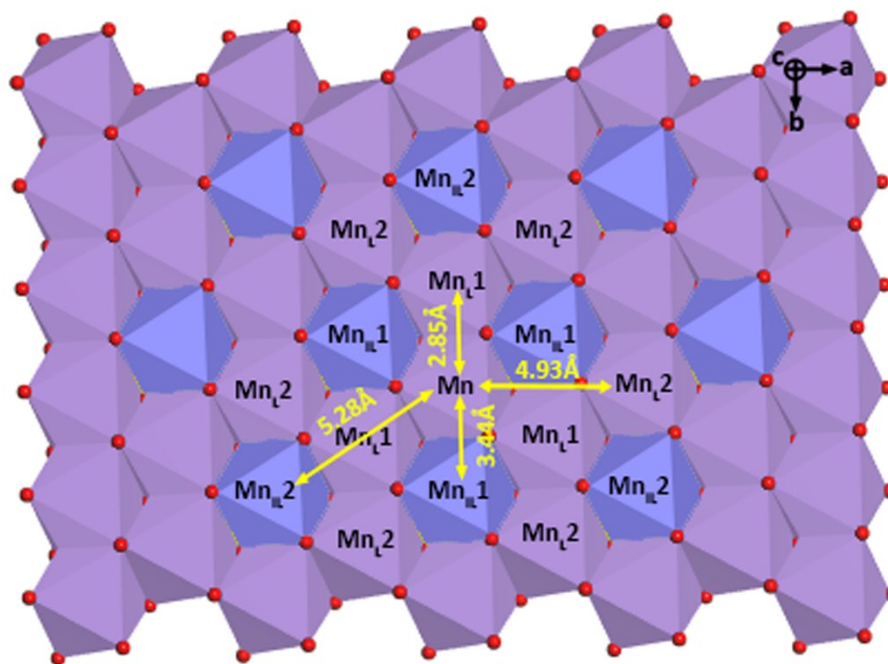
Figure S6. Scheme of a δ-MnO$_2$ layer which containing 1/3 vacancy (blue octahedral) per layer octahedron, seen along c-axis. The Mn$_L$X (X = 1, 2 or 3) means the first, second and third Mn shells around a given Mn. The Mn$_{IL}$Y (Y= 1 or 2) means pairs formed by layer Mn and Mn at vacancies belonging respectively to the first and second shells.
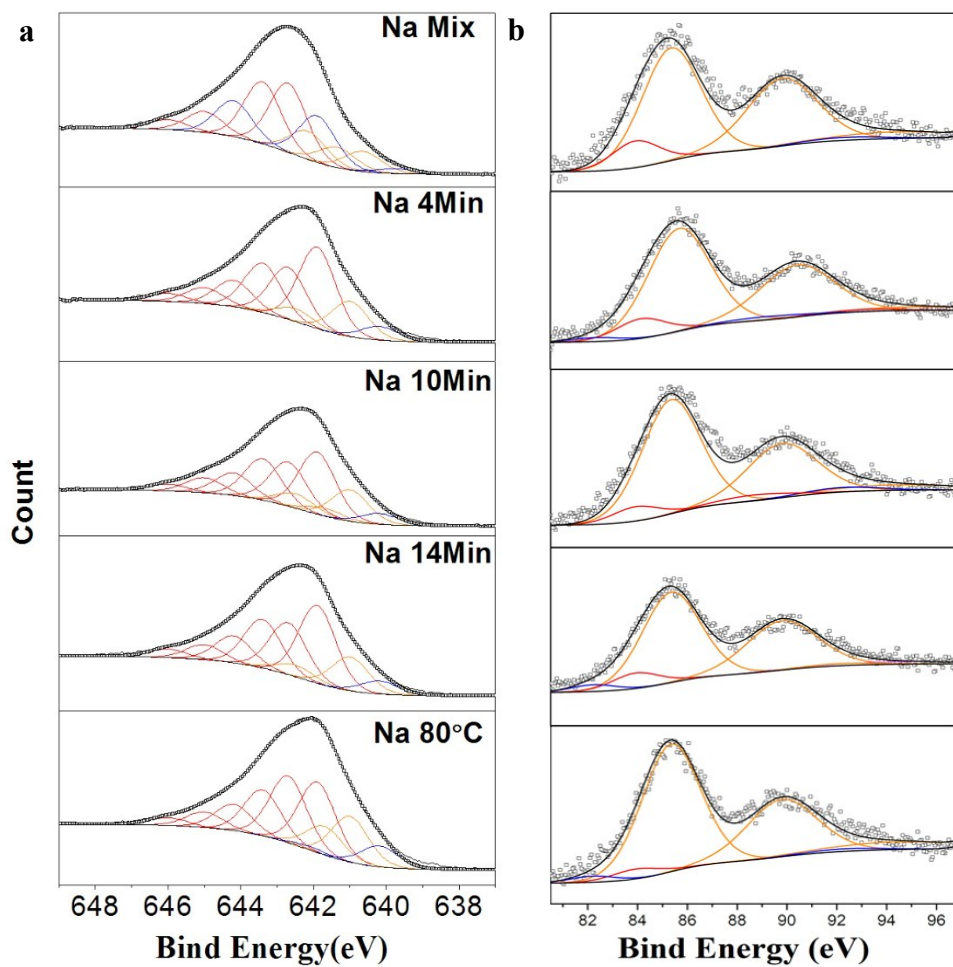
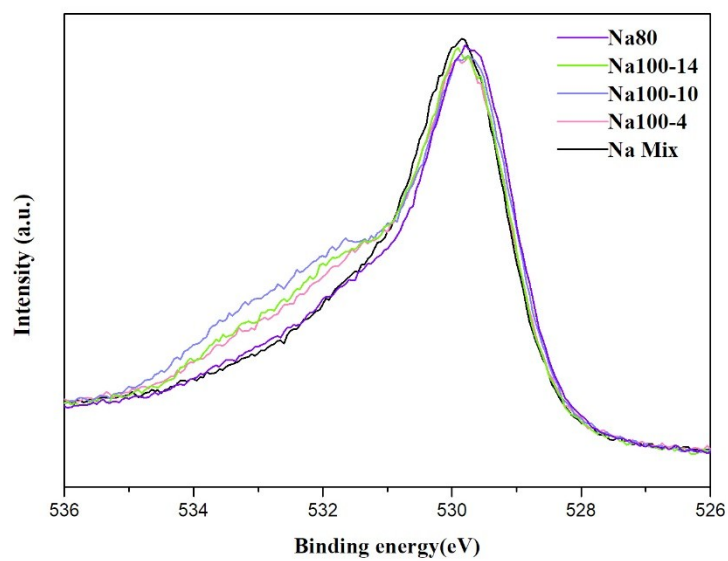**Figure S7.** XPS broad scans of (a) Mn 2p$_{3/2}$ and (b) Mn 3s spectra of intermediate products at NaMix, Na100-4, Na100-10, Na100-14, and Na80.

Figure S8. Oxygen 1s spectra of intermediate products at different intervals of Na+ stabilized α-MnO$_2$ formation and crystal growth;
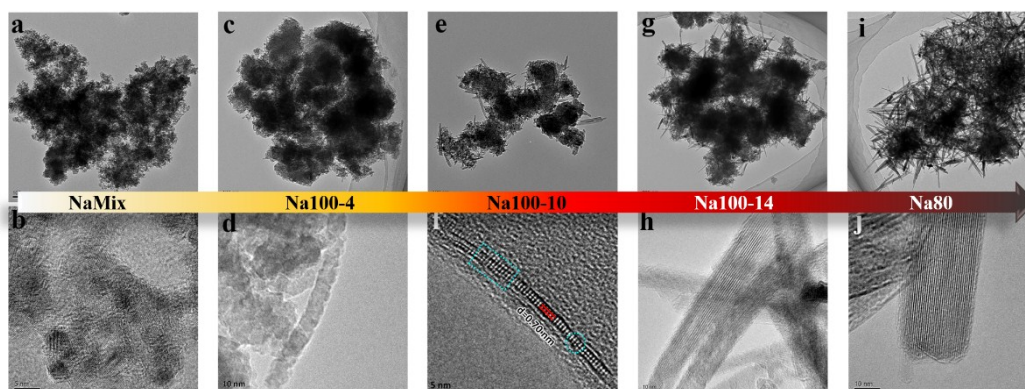

Figure S9. The TEM and HRTEM images during entire synthetic process: (a, b) NaMix, (c, d) Na100-4, (e, f) Na100-10, (g, h) Na100-14 and (i, j) Na80.
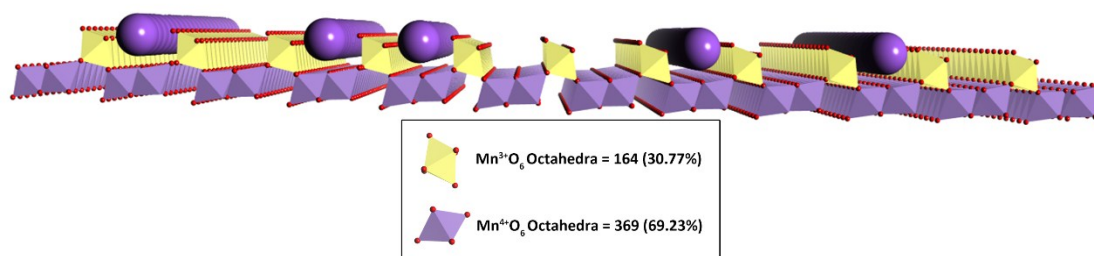
Figure S10. Schematic illustrating the ideal structure of δ-MnO_2 which can assemble to α-MnO_2.
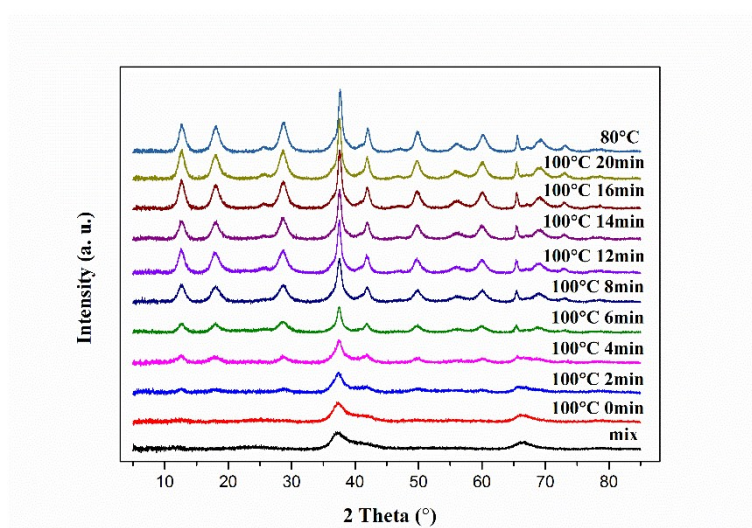
Figure S11. XRD patterns of intermediate products at different intervals of K$^+$ stabilized α-MnO$_2$ formation and crystal growth;
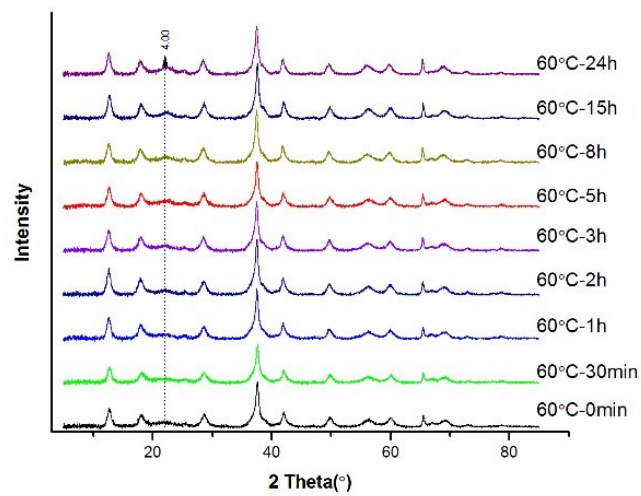
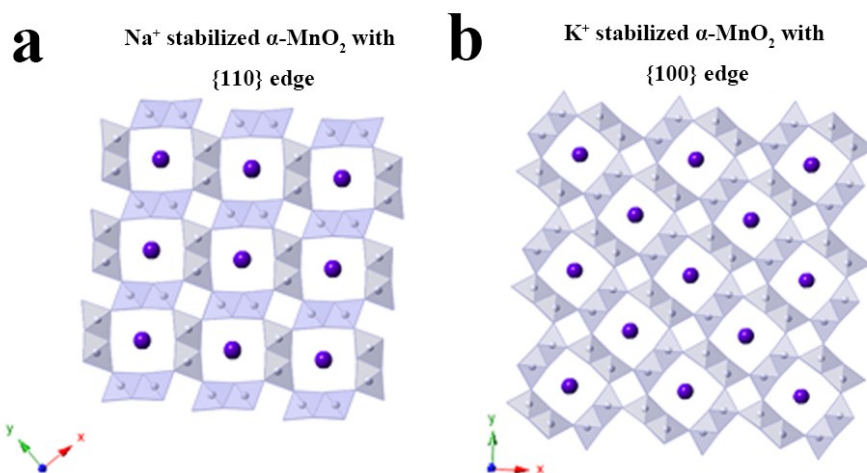**Figure S12.** XRD patterns of intermediate products at different intervals of Na^+ stabilized α-MnO_2 age under 60 ℃.

Figure S13 the calculated relaxed (a) Na^+ stabilized α-MnO_2 structure and (b) K^+ stabilized α-MnO_2 structure.

Supporting Tables

Table S1. K^+ content, average oxidation states (AOS) of Mn in intermediate products at various time intervals during K^+-stabilized α-MnO_2 formation obtained from titration and fittings of Mn ($2p^{3/2}$)

Samples	XPS ($\pm$ 0.02)	Titration	K^+ content (% mol)
KMix	3.80	3.95 $\pm$ 0.03	6.91 $\pm$ 0.13
K100-0	3.77	3.90 $\pm$ 0.01	4.85 $\pm$ 0.09
K100-2	-	3.85 $\pm$ 0.01	39.57 $\pm$ 0.15
K100-4	3.74	3.80 $\pm$ 0.02	5.25 $\pm$ 0.11

K100-10	3.80	3.87 ± 0.04	5.89 ± 0.04
K100-20	-	3.85 ± 0.02	8.51 ± 0.03
K80	3.80	3.82 ± 0.03	10.56 ± 0.08

Table S2. Near-surface compositions of Mn and O species derived from fittings of Mn (2p3/2) and O (1s).

Sample	Mn(III) (±0.003)	Mn(II) (±0.001)	Mn(IV) (±0.003)	O^{2-}	OH^-	H_2O
KMix	0.158	0.037	0.845	0.661	0.183	0.156
K100-0	0.149	0.037	0.814	0.645	0.196	0.159
K100-4	0.153	0.049	0.798	0.580	0.218	0.202
K100-10	0.112	0.039	0.849	0.640	0.210	0.150
K80	0.137	0.028	0.835	0.770	0.161	0.068